

Atomic-Level Changes during Electrochemical Cycling of Oriented LiMn_2O_4 Cathodic Thin Films

Yumi H. Ikuhara,* Xiang Gao, Kazuaki Kawahara, Craig A. J. Fisher, Akihide Kuwabara, Ryo Ishikawa, Hiroki Moriwake, and Yuichi Ikuhara

HPSTAR
1384-2022



Cite This: *ACS Appl. Mater. Interfaces* 2022, 14, 6507–6517



Read Online

ACCESS |



Metrics & More



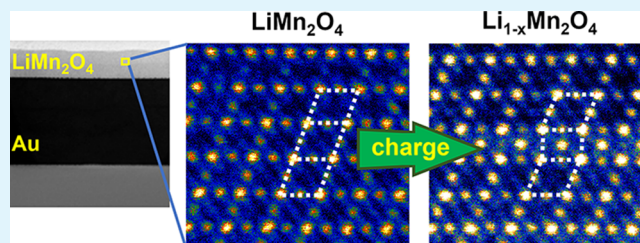
Article Recommendations



Supporting Information

ABSTRACT: Spinel LiMn_2O_4 is an attractive lithium-ion battery cathode material that undergoes a complex series of structural changes during electrochemical cycling that lead to rapid capacity fading, compromising its long-term performance. To gain insights into this behavior, in this report we analyze changes in epitaxial LiMn_2O_4 thin films during the first few charge–discharge cycles with atomic resolution and correlate them with changes in the electrochemical properties. Impedance spectroscopy and scanning transmission electron microscopy are used to show that defect-rich LiMn_2O_4 surfaces contribute greatly to the increased resistivity of the battery after only a single charge. Sequences of $\{111\}$ stacking faults within the films were also observed upon charging, increasing in number with further cycling. The atomic structures of these stacking faults are reported for the first time, showing that Li deintercalation is accompanied by local oxygen loss and relaxation of Mn atoms onto previously unoccupied sites. The stacking faults have a more compressed structure than the spinel matrix and impede Li-ion migration, which explains the observed increase in thin-film resistivity as the number of cycles increases. These results are used to identify key factors contributing to conductivity degradation and capacity fading in LiMn_2O_4 cathodes, highlighting the need to develop techniques that minimize defect formation in spinel cathodes to improve cycle performance.

KEYWORDS: thin-film battery, cathode material, LiMn_2O_4 spinel, chemical solution deposition, scanning transmission electron microscopy, stacking fault, surface degradation, structure–property relationships



1. INTRODUCTION

Lithium-ion batteries (LIBs) are ubiquitous energy storage devices used in portable electronics, power tools, hybrid electric vehicles, and, increasingly, large-scale stationary applications because of their high energy and power densities.^{1–4} For all these applications, next-generation LIB materials need to be developed to increase cycle life, safety, recyclability, and power density at reduced cost.^{5–7} As the stability of an LIB during cycling ultimately depends on the integrity of the electrode materials during lithium deintercalation and reintercalation (which can be compromised even at low potentials, particularly at interfaces), considerable effort continues to be directed toward understanding the degradation mechanisms in greater detail.^{7–10}

It is generally understood that the surface of an oxide is inherently less stable than the crystal interior because of the lower (meaning incomplete and strongly anisotropic) coordination environments of surface atoms and their exposure to different chemical species, and thus, surface layers are likely to be the first to degrade. However, the structure and composition of the crystal bulk, especially the ease of formation of internal defects, phase separation, dopant segregation, and other microscopic phenomena,^{10–13} may

also contribute in varying degrees to a decline in performance of the cathode material and, thus, the battery as a whole.

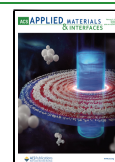
Spinel LiMn_2O_4 (LMO) has long been considered a promising cathode material for next-generation LIBs because of its high operating voltage (4.1 V vs Li/Li^+), low toxicity, good stability, and low cost^{14–16} compared to conventional layered materials such as LiCoO_2 , $\text{Li}(\text{Ni},\text{Co},\text{Mn})\text{O}_2$, and $\text{Li}(\text{Ni},\text{Co},\text{Al})\text{O}_2$. An even higher operating voltage (4.7 V vs Li/Li^+) is obtained by partially replacing Mn with Ni, e.g., $\text{LiNi}_{0.5}\text{Mn}_{1.5}\text{O}_4$.^{17,18} Despite these advantages, LiMn_2O_4 -based cathodes are still not widely used because they typically exhibit rapid capacity fading.^{19–21}

Several studies have been carried out to identify the cause of capacity fading, with various mechanisms having been identified.^{10,12,22–24} The majority of these have focused on the surfaces of LMO particles (or, more recently, thin films) because these are known to change markedly during

Received: September 27, 2021

Accepted: January 13, 2022

Published: January 27, 2022



electrochemical cycling in response to various physicochemical interactions with the liquid electrolyte.²² In particular, Mn-ion dissolution from the cathode into the nonaqueous liquid electrolyte,^{10,12,25–28} Jahn–Teller distortion associated with the cubic-to-tetragonal phase transition when cycled below 3 V,¹⁴ and cation mixing²³ have been cited as factors strongly affecting the reversibility of Li-ion intercalation, contributing to poor cyclability.

Although these studies have provided remarkable insights into the electrode–electrolyte interfacial behavior, several aspects of the degradation mechanisms remain uncertain, particularly those involving structural changes within the cathode and how these relate to changes at the surfaces. Understanding such complex processes at a fundamental (i.e., atomic) level is an important step in identifying strategies to limit capacity fade and develop improved cathode materials, especially those with spinel-type structures. Thin-film cathodes are well-suited for this because they allow greater control over microstructure and crystal orientation, which allows model systems to be prepared reproducibly and more practically than, e.g., multifaceted particles or single crystals, so they were chosen for this work.

LMO cathodic thin films for all-solid-state or miniaturized LIBs can be synthesized by a variety of techniques, including sputtering,^{29–32} pulsed laser deposition,^{33–38} electrostatic spray deposition,^{39,40} and chemical solution processing.^{24,41} Chemical solution deposition (CSD) in particular is a versatile non-vacuum process that offers a number of advantages over other methods such as low cost, close stoichiometry control, and environmental friendliness.⁴² By optimizing the processing parameters, single-phase LMO can be crystallized at low temperature, minimizing the amount of Li lost to volatilization, and thus, the same CSD method used in our previous work on cathode–electrolyte and cathode–substrate interfaces was chosen to prepare (111) oriented LMO thin films for this study.^{24,41}

Here, we investigate the changes in oriented LMO cathode films at the atomic level using scanning transmission electron microscopy (STEM) at different stages of electrochemical cycling. Atomic-level structures were determined from high-angle annular dark-field (HAADF) and annular bright-field (ABF) observations,^{43,44} and changes in Mn valence states were deduced from electron energy loss spectroscopy (EELS) measurements at the surface and inside the film. Changes in structure and composition were correlated with changes in electrochemical properties derived from impedance measurements using a Metropolis algorithm for equivalent circuit fitting. In particular, we observed the formation of characteristic {111} stacking faults in the spinel structure upon Li delithiation (charging), determining the atomic structure of the stacking faults by imaging in two directions. Despite appearing to be reversible after the first cycle, the number and concentration of these stacking faults increased markedly with further cycling. The increased resistance of the film bulk to Li-ion transport suggests that they play a significant role in decreasing capacity of the material.

2. EXPERIMENTAL SECTION

2.1. Thin Film Deposition. Epitaxial (111) LiMn₂O₄ thin films were chosen as model systems for this study because the small misfit between (111) surfaces of the Au substrate and LiMn₂O₄ allows high-quality films to be prepared with minimal distortion to the lattice vis-a-vis a single crystal. The (111) surface is also known to be the most

stable,^{38,45} making it easier to prepare atomically flat, well-defined surfaces amenable to atomic-level analysis. The thin films were prepared using the identical method to our earlier studies on LiMn₂O₄,^{23,24,41} so only a brief outline will be given here. Metal-organic precursors LiOCH(CH₃)₂ and Mn(OC₃H₇)₂ were each dissolved in 2-ethoxyethanol (C₂H₅OC₂H₄OH or EGMEE) solvent and refluxed at 135 °C for 3 h under a dry N₂ atmosphere. After cooling to room temperature, each solution was condensed in a rotary evaporator to remove the (CH₃)₂CHOH byproduct. A homogeneous metal-organic [Li–Mn–O] precursor solution was then prepared by mixing the two solutions together, with fresh EGMEE added to lower the viscosities to a suitable level, followed by refluxing at 135 °C for 1 h. The combined precursor solution was deposited by spin coating onto Au-coated Al₂O₃ (0001) substrates at a spinning speed of 2000 rpm for 20 s under flowing nitrogen gas. The LMO precursor films were then calcined at 200 °C for 30 min to remove the organic ligands and annealed at 750 °C for 1 h in oxygen.⁴¹ To obtain thicknesses greater than 100 nm, the coating and heating steps were repeated several times. X-ray diffraction (XRD) measurements of the heat-treated films were performed with Cu K_α radiation using a Rint2000 (Rigaku, Tokyo, Japan) diffractometer equipped with a monochromator and operated at 40 kV and 50 mA.

2.2. Electrochemical Measurements. For electrochemical characterization, the cathodic half-cells were transferred to a glove box under an Ar atmosphere and a cell constructed using lithium metal as the anode and a mixture of propylene carbonate and 1 M LiClO₄ as the electrolytic solution. Cyclic voltammograms (CV) of the cells were obtained using a Biologic VMP-3 potentiostat at 25 °C. Electrochemical impedance spectroscopy measurements were carried out over a frequency range from 10⁵ to 10^{–2} Hz at different potentials.

Electrochemical impedance data were fitted using a Monte Carlo algorithm.^{46,47} During curve fitting, the objective function (χ^2) was minimized according to

$$\chi^2 = \frac{1}{2T} \sum |Z_{\text{exp}}(\omega) - Z_{\text{fit}}(\omega)|^2 \quad (1)$$

where Z_{exp} and Z_{fit} are experimental and theoretical impedance spectra, ω is the frequency, and T is the noise variance estimated from the imaginary part of the impedance plot, $\text{Im } Z_{\text{exp}}(\omega)$, when ω is larger than 10⁵ Hz. We used a random-walk Metropolis–Hastings algorithm to analyze the spectra and identify the global minimum of χ^2 . One of the advantages of curve fitting using this algorithm is that the statistical significance of the difference between two values can be judged by plotting histograms of parameters that pass the Metropolis test. The number of Monte Carlo sweeps used was 1.1×10^6 with a 10⁵ iteration “burn-in” period. Details of the curve-fitting method used are described elsewhere.⁴⁶

2.3. Microscopic Observations. Thin-film samples were prepared by separating LMO cathodes on Au/Al₂O₃ substrate from the cells and coating them with a protective layer of amorphous carbon (~50 nm). Cross-sectional specimens for TEM and STEM observations were prepared using a dual-beam focused ion beam scanning microscope (NB5000, Hitachi, Japan) with Ga ions at an accelerating voltage from 40 to 2 kV followed by ion milling (Gatan 691, Gatan, USA) at 1.5 to 0.5 kV, cooling with liquid nitrogen, and lastly, argon plasma cleaning (Solarus 950, Gatan, USA) to completely remove any residual amorphous film.

A conventional 300 kV JEM-3000F microscope (JEOL Ltd., Japan) was used for selected-area electron diffraction (SAED) and HREM observations. A 200 kV JEM-2100F microscope (JEOL Ltd., Japan) equipped with a spherical-aberration corrector (CEOS GmbH) was utilized for angle-resolved STEM imaging. A convergence angle of 25 mrad and a dwell time of 20 μ s, together with annular dark-field detector inner/outer angles of 70/240 and 29/70 mrad for HAADF and LAADF imaging, respectively, and annular bright-field detector inner/outer angles of 9/25 mrad for ABF imaging were used.

STEM-EELS analysis was carried out using a JEM-ARM200F microscope (JEOL Ltd., Japan) equipped with a spherical-aberration corrector (CEOS GmbH, Germany), a Gatan Image Filter (GIF), and a Wien filter-type monochromator. An accelerating voltage of 120 kV

and an entrance aperture of 2.5 mm were selected in all cases. EELS spectra were recorded by scanning a comparatively large area in STEM mode with an energy resolution of 0.3 eV; settings of 0.05 eV/channel and an integration time of 0.2 s per readout were used for Li-K and Mn-M_{2,3} edges, and a 0.1 eV/channel and an integration time of 1 s per readout were used for O-K and Mn-L_{2,3} edges. The energy resolution was determined by measuring the full-width at half maximum of the zero-loss peak.

In the ideal LMO spinel (*Fd3m*) unit cell, Li and Mn atoms occupy the tetrahedral 8a and octahedral 16d positions, respectively, with O atoms on 32e sites; when viewed along $\langle 110 \rangle_{\text{LMO}}$ projections, all columns contain atoms of only one type, with Mn columns arranged in a diamond configuration.⁴⁸ Another projection with columns of only one element type is $[\bar{1}12]_{\text{LMO}}$, which lies normal to $[110]_{\text{LMO}}$. The $[\bar{1}10]_{\text{LMO}}$ projection was thus chosen for the majority of structure analyses in this study, with the $[\bar{1}12]_{\text{LMO}}$ projection used to obtain data in the third dimension for a number of delithiated (fully charged) samples.

3. RESULTS AND DISCUSSION

3.1. Electrochemical Properties. Figure 1 shows a schematic of an Au-Al₂O₃ substrate/LMO cathode/electro-

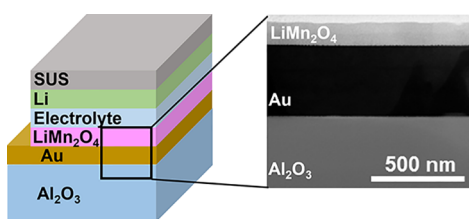


Figure 1. Schematic of a spinel LiMn₂O₄ thin-film battery grown on an Au(111)/Al₂O₃(111) single-crystal substrate with a cross-sectional bright-field TEM image of the cathode side.

lyte/Li anode thin-film cell together with a cross-sectional bright-field TEM (BF-TEM) image showing a magnified view of the cathodic half of an actual cell fabricated using CSD. The top surface of such a thin film grows preferentially with a (111) orientation on the Au(111)/Al₂O₃(111) substrate. Cyclic voltammograms of this cell reported in a previous work²³ revealed two delithiation peaks at around 4.03 and 4.17 V during the charge half-cycle and lithiation peaks at 3.99 and 4.09 V during the discharge half-cycle, confirming the reversibility of the Li (de)intercalation process. The two peaks of each process are characteristic of the spinel structure and indicate that Li ions are extracted and inserted between LiMn₂O₄ and λ -MnO₂ (spinel) phases in two steps, which is consistent with previous reports.⁴⁹ Measurements of the decrease in area enclosed by the CV curves indicate a capacity fade of around 8% after only four charge–discharge cycles.²³

In this study, impedance spectroscopy was used to characterize the different components of the cell and determine the changes in resistance with cycling. Typical spectra at different potentials during the first charge of the thin-film battery are plotted in Figure 2a. The spectrum at 3.0 V, taken before delithiation commenced, shows a small arc in the high-frequency region and a slightly inclined line in the low-frequency region, indicating the blocking character of the fully lithiated electrode. When the potential was increased to 4.05 V, a second arc appears in the middle-frequency region, and this becomes more distinct at a potential of 4.2 V. As the process of delithiation during charging involves a sequence of complex phenomena (viz., (i) Li-ion diffusion through the LMO film, (ii) charge transfer across the cathode/electrolyte

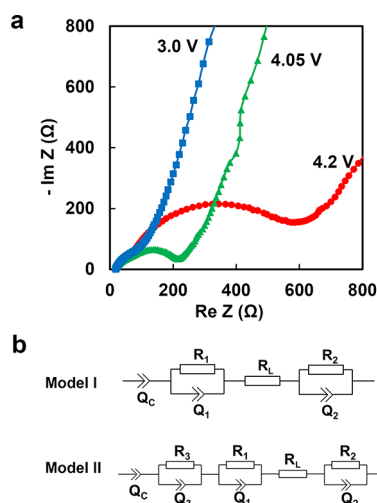


Figure 2. (a) Impedance spectra from an Au/LiMn₂O₄/electrolyte/Li cell measured after a single charge at 3.0 V (blue squares), 4.05 V (green triangles), and 4.2 V (red circles). (b) Two possible equivalent circuit models: Q = capacitance, R = resistance, C = LMO/Au interface, 1 = thin-film/electrolyte interface, L = electrolyte, 2 = Li/electrolyte interface, and 3 = LMO-film bulk.

interface, and (iii) Li-ion transport within the electrolyte solution), to analyze these spectra, we constructed two candidate equivalent circuit models, model I and model II, as illustrated in Figure 2b.

Model I consists of two parallel components corresponding to (i) Li-ion transfer across the film/electrolyte interface and (ii) Li-ion transfer from electrolyte to the Li-metal anode. Here, R_L, R₁ and R₂ are, respectively, the resistance of the liquid electrolyte, the resistance of the interface between LMO film and electrolyte (affected strongly by the state of the LiMn₂O₄ surface) and the resistance of the interface between Li anode and electrolyte (predominantly affected by the state of the Li-metal surface).

In model II, there is an additional parallel component in which R₃ is the resistance of the LMO thin film to Li-ion migration. The ohmic resistance (R_L), i.e., electrolyte resistance, is given by the intercept on the Re Z axis. In these models, the capacitances of the LMO surface, the Li surface, the LMO bulk, and the interface between LMO and Au are represented by the constant phase elements Q₁, Q₂, Q₃, and Q_c, respectively.

Electrochemical impedance data at 3.0, 4.05, and 4.2 V during the first charge are plotted separately in Figure 3a–c, together with their fitted curves. As seen in Figure 3d, the histograms of χ^2 calculated using model I and model II for the spectrum in Figure 3a overlap, which means that model II is overfitting the data, and thus, we chose model I to describe the data before charging. In contrast, at 4.05 V (Figure 3b) and 4.2 V (Figure 3c), model II gives the better fit since χ^2 is smaller than that of model I in these cases (Figure 3e,f).

Experimental and fitted impedance spectra with χ^2 plots for the LMO film after its fifth charge to 4.2 eV are shown in Figure 4. In this case, the experimental spectrum was also better fitted (smaller χ^2) to the simulated spectrum of model II (Figure 4a) than that of model I (Figure 4b).

The quantitative results for the various equivalent circuit components in all four cases are summarized in Table 1. These values show that, with increasing potential voltage, the resistances of the electrolyte (R_L) and Li/electrolyte interface

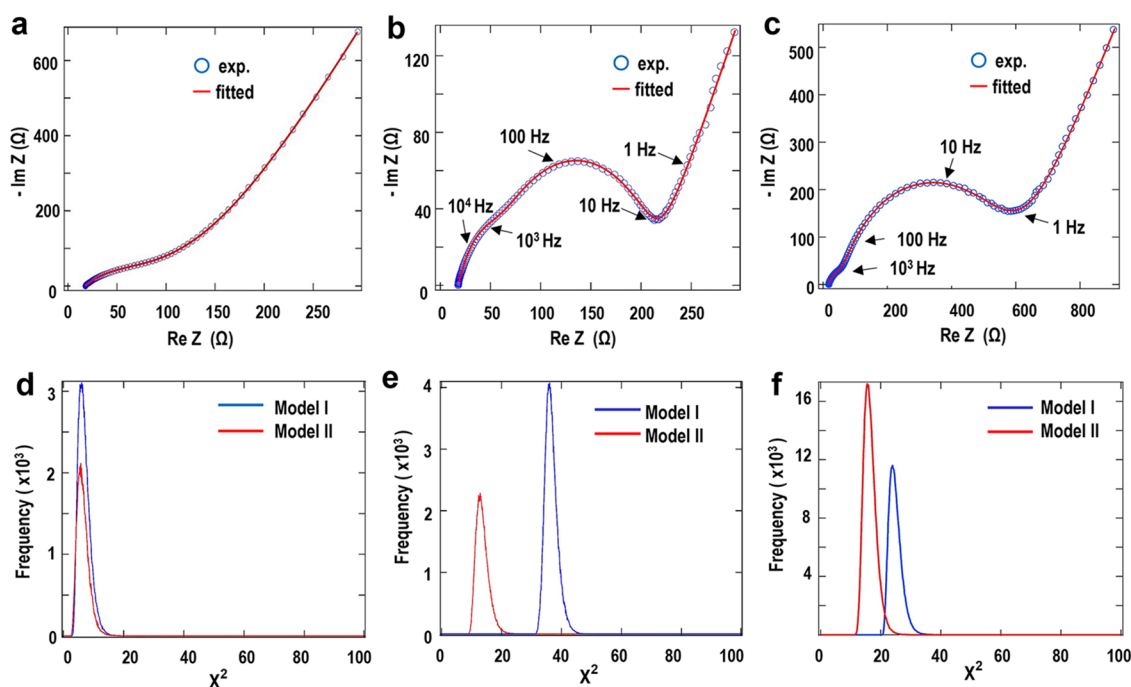


Figure 3. Comparison between experimental (circles) and fitted (lines) impedance spectra of an Au/LiMn₂O₄/electrolyte/Li cell after a single charge at (a) 3.0 V, (b) 4.05 V, and (c) 4.2 V. Histograms obtained from Metropolis tests of model I and model II for the corresponding spectra at (d) 3.0 V, (e) 4.05 V, and (f) 4.2 V.

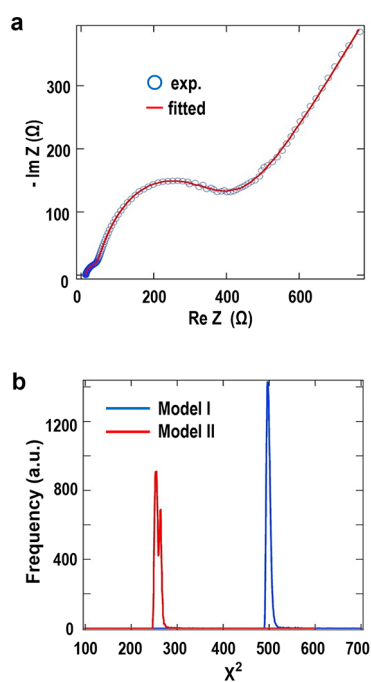


Figure 4. (a) Comparison between experimental (circles) and fitted (lines) impedance spectra of an Au/LiMn₂O₄/electrolyte/Li cell after the fifth charge at 4.2 V. (b) Histograms obtained from Metropolis tests of models I and II.

(R_2) remain essentially unchanged. In contrast, the resistance at the film/electrolyte interface (R_1) increased from 116 to 140 to 489 Ω when the voltage was increased from 3 V (fully lithiated) to 4.05 V (partially delithiated) to 4.2 V (mostly delithiated) before decreasing again after the fifth charge. The large increase after the first charge indicates that the greatest disruption to the surface structure and chemistry occurs once

Table 1. Estimated Resistances (in Ω) of Components of an Au/LiMn₂O₄/Electrolyte/Li Cell at Various Stages of Electrochemical Cycling

charge state (V)	cycle no.	R_1	RL	R_2	R_3
3.0	-	116	16.9	35.1	-
4.05	1	139.6	16.8	31.2	23.6
4.2	1	489	17.3	44.2	44.9
4.2	5	242	12.6	26.7	103

most of the Li has been removed for the first time. The LMO film internal resistance (R_3) also increased from 24 Ω to around 100 Ω after only five charge cycles, suggesting that further structural changes took place.

3.2. Crystal Structure Changes. Simultaneous high-resolution HAADF and ABF imaging revealed details about the structural changes caused by Li extraction and reinsertion during electrochemical cycling. The cross-sectional HAADF micrographs in Figure 5 show low-magnification views of the LMO cathode and Au current collector down the $[1\bar{1}0]_{\text{LMO}}$ zone axis before and after different numbers of charge cycles. The Mn ($Z = 25$) columns in the film appear as bright contrast, but the much heavier Au ($Z = 79$) atoms in the substrate are too bright to be distinguishable at the same time as Mn columns, and thus, the Au substrate appears as a white slab.^{24,41} In the pristine film (Figure 5a), the contrast is uniform with no visible defects, whereas brighter layers appear parallel to $(111)_{\text{LMO}}$ and $(\bar{1}\bar{1}\bar{1})_{\text{LMO}}$ planes in the single-charged film (Figure 5b); these correspond to stacking faults in the spinel structure roughly one Mn diamond unit wide and represent about 1.4% of all Mn diamond layers. The $(\bar{1}\bar{1}\bar{1})_{\text{LMO}}$ (oblique) stacking faults appear to initiate from terrace steps on the $(111)_{\text{Au}}$ substrate (see Supporting Information Figure S1 for higher magnification images of the LMO/Au interface). As steps act as stress concentrators, this suggests that stacking

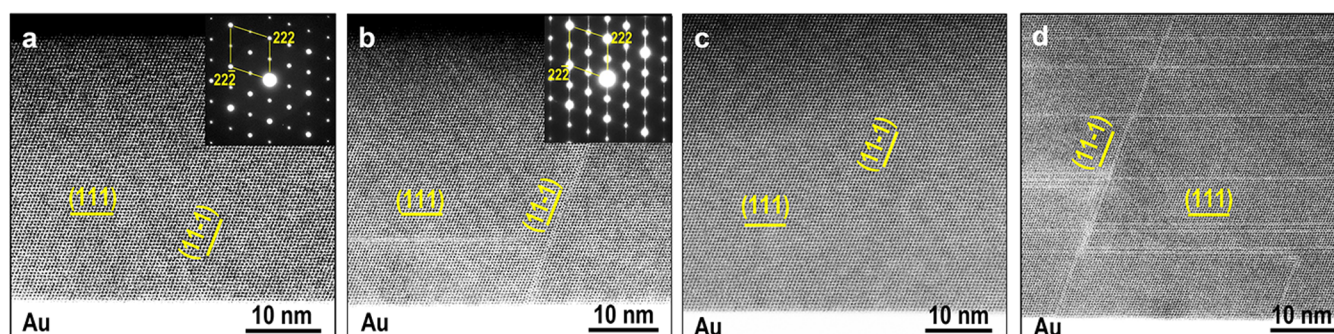


Figure 5. HAADF images taken along $[1\bar{1}0]_{\text{LMO}}$ zone axes (a) before cycling, (b) after a single charge ($@0.1$ mV/s), (c) after a single charge–discharge ($@0.1$ mV/s), and (d) after five charges ($@1$ mV/s). Insets in (a) and (b) show SAED patterns of the films.

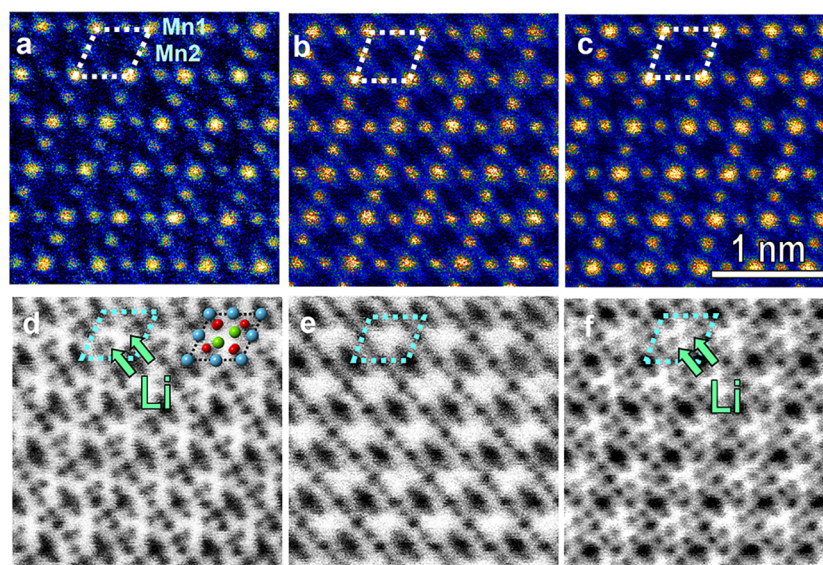


Figure 6. Atomic-resolution (a–c) HAADF and (d–f) ABF images of LiMn_2O_4 epitaxial films before charging (pristine), after a single charge, and after a single charge–discharge cycle, respectively, viewed along $[1\bar{1}0]_{\text{LMO}}$, with a structure model overlaid in (d). Mn1 columns lie at the corners of the dotted diamonds, and Mn2 columns lie midway along their edges.

faults are particularly prone to formation at sites of increased strain in the spinel lattice.

The single-layer stacking faults account for the diffuse streaks connecting the $\{111\}_{\text{LMO}}$ spots observed in the corresponding SAED images in the inset of Figure 5b. In contrast, the film in Figure 5c after the first charge–discharge cycle once again exhibits a stacking fault-free nanostructure similar to that of the pristine film. Despite this, after the fifth charge, many more stacking faults (7.7% of all Mn diamond layers in the image) have formed, especially parallel to the substrate. This suggests that a small concentration of lattice defects remains even after full discharge, steadily accumulating so that the formation of stacking faults becomes easier and less reversible as the number of charge–discharge cycles increases. An increasing portion of the cathode will thus be converted to the stacking fault structure after many charge–discharge cycles. It is not yet known why interstitial Mn defects accumulate in some layers and not others, but as suggested by the association of oblique stacking faults with terrace steps, it is likely a function of local differences in lattice strains, point defect concentrations, or Li/Mn^{*+} concentration gradients as Li is being removed. The cumulative damage caused by repeated formation and elimination of stacking faults with the associated

volume changes can be expected to have a strong effect on the electrochemical and mechanical properties of the film.

Figure 6a–c shows higher magnification cross-sectional HAADF images of the pristine, single-charged, and single-discharged LMO film, respectively, viewed down $[1\bar{1}0]_{\text{LMO}}$, i.e., perpendicular to the images in Figure 5. In these Z-contrast images, the bright Mn ($Z = 25$) columns are readily distinguished; Mn1 columns are brighter than Mn2 columns because the former have atom densities twice that of the latter. No contrast is visible at 8a or 32e positions, as expected if occupied by lighter elements Li ($Z = 3$) and O ($Z = 8$).

In the corresponding ABF image of the pristine sample in Figure 6d, all elements, including light elements Li and O, are visible; as an example, the arrows show that two Li columns are distinguishable within an Mn diamond unit. After a single charge to 4.2 V, however, no contrast is detectable on Li sites as seen in the ABF STEM image in Figure 6e. This latter observation confirms that the structure has changed from the spinel structure of LMO to that of λ - MnO_2 , with the Li concentration below the detection limit. When the cell is discharged to 3.0 V, Li atoms return to the Li 8a sites within the Mn diamonds as seen in Figure 6f.

3.3. LiMn_2O_4 Surface Structure Evolution. The HAADF images in Figure 7 show that the structure at the thin-film

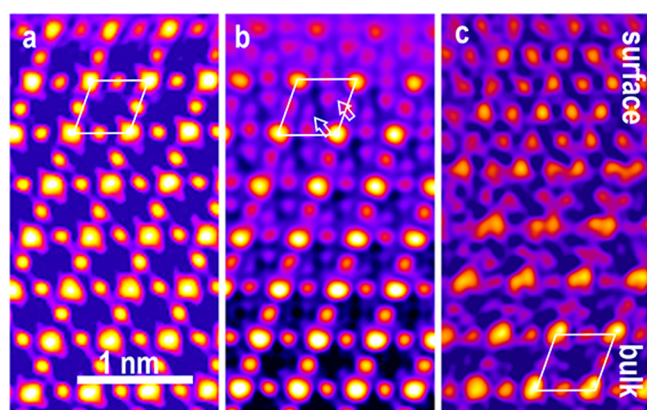


Figure 7. Structure degradation at (111) surfaces of LiMn_2O_4 thin films during electrochemical cycling revealed by high-resolution HAADF imaging: (a) before cycling, (b) after the first charge to 4.2 V, and (c) after the fifth charge to 4.2 V.

surface also undergoes substantial changes during electrochemical cycling. In Figure 7a, the arrangement of atom columns in the surface region of the film before cycling is identical to that in the bulk (in Figure 6a), indicating a homogeneous crystal structure from the surface to the film interior. In contrast, the single-charged film in Figure 7b has a thin surface layer approximately 2 nm thick with bright contrast at spinel 8a sites as indicated by two arrows corresponding to the presence of Mn atoms on Li sites (anti-site Mn_{8a} or Mn_{Li} defects), forming an Mn_3O_4 -like configuration when observed down $[11\bar{1}]_{\text{Mn}_3\text{O}_4}$. At the same time, the contrast of the Mn1 and Mn2 columns decreases markedly in the outermost layer in Figure 7b. This is consistent with dissolution of Mn into the electrolyte; earlier studies showed that the formation of Mn_3O_4 results from the loss of O ions to the organic electrolyte, and disproportionation of the resulting Mn^{3+} ions produces highly soluble Mn^{2+} ions.^{10,28,50} In subsurface layers below the Mn_3O_4 layers, the relative brightness of Mn2 columns decreases compared with those in the pristine sample (Figure 7a), suggesting that the Mn_{Li} atoms are predominantly from Mn2 columns. As Mn_3O_4 is a poor Li-ion conductor, this cation mixing at the surface is expected to increase the resistivity of the cathode–electrolyte interface, which is consistent with the results in Table 1.

After the fifth charge, surface degradation has progressed with further loss of O. Figure 7c shows that this results in a defect-rich surface with a significant fraction of Mn atoms on 16c sites in the topmost 2 nm, which essentially means that a rock-salt structure has formed with a denser packing of cations and anions. As rock-salt MnO does not conduct Li ions, this is expected to further increase the resistance of the interface, but this thin phase, like the rest of the surface, is deficient in Mn and O. These vacancies may then provide some pathways for Li to diffuse into the bulk. Our atomic-level HAADF observations and impedance results thus suggest that the increased resistivity of the interface is related to formation of the Li-blocking Mn_3O_4 -like and rock-salt phases at the surface. Mn^{2+} dissolution and loss of oxygen has also been shown to accompany surface degradation during cycling.²³ The reason for the decrease in cathode/electrolyte resistance after the first cycle is not discernible from the present results, but it may well be related to the well-known phenomenon of “conditioning,” which occurs after several cycles of battery as an electric double layer and permeable cathode–electrolyte interface^{51–53} is established, which allows faster Li-ion transfer than when the surface is delithiated for the first time.

3.4. Stacking Fault Formation. Figure 8a,b shows HAADF and ABF images, respectively, of a region of a thin film containing a (111) stacking fault parallel to the film–substrate interface after its initial charge to 4.2 V. Jahn–Teller distortion of the MnO_6 octahedra is evident from the shorter and longer O–Mn–O distances in Figure 8b, suggesting that Mn ions at their centers are in the trivalent state. The dashed rectangles highlight a repeat unit of the stacking fault, which forms a coherent interface with the matrix spinel structure (dashed diamonds) on either side. Based on changes in Mn2 contrast within the stacking fault layers, the stacking fault appears to have formed as a result of Mn2 atoms at the side edges of Mn diamonds relaxing to the diamond centers (Mn3 sites) in the absence of Li atoms. This is similar to the rock-salt structure at the film surface observed after five charges but with the structure compressed in the $[11\bar{1}]_{\text{LMO}}$ direction and the Jahn–Teller MnO_6 octahedra flipped across the $(1\bar{1}2)$ mirror plane (Figure 8c).

The thickness of each $(111)_{\text{LMO}}$ layer of the HAADF image in Figure 8a is plotted in Figure 8d. The average thickness of the spinel layers is about 0.466 nm (close to that of the fully lithiated spinel at around 0.476 nm), and the thickness of the stacking fault layer is 0.403 nm. The height of the stacking fault

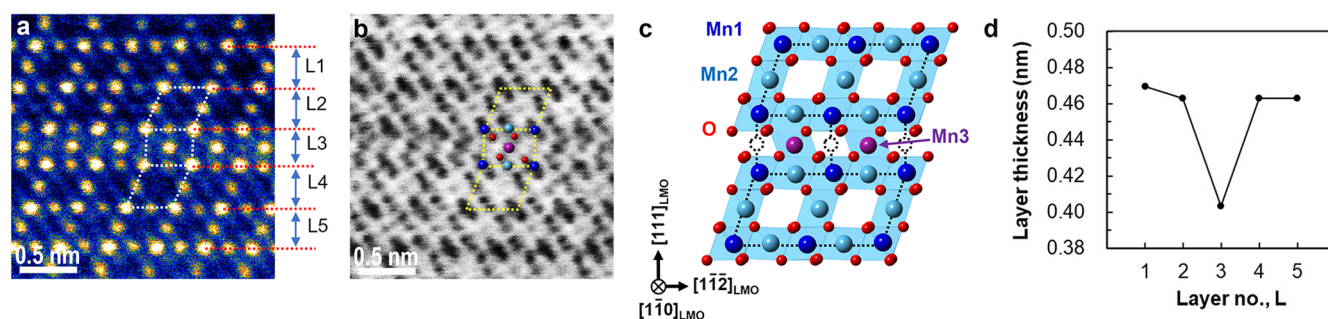


Figure 8. (a) HAADF and (b) ABF images of a stacking fault in an epitaxial LMO film after a single charge to 4.2 V viewed down $[1\bar{1}0]_{\text{LMO}}$. Mn2 columns contain half the number of atoms as Mn1 columns and thus have weaker contrast. (c) A model of the stacking fault structure, with dashed lines indicating the Mn-sublattice repeat units and dashed circles indicating Mn2 sites with low occupancy. Mn1 atoms are dark blue, Mn2 atoms are light blue, Mn3 atoms are purple, and O atoms are red. Mn3 sites at the centers of repeat units in the stacking fault layer have occupancies midway between those of Mn1 and Mn2 sites. (d) Plot of layer thickness across the stacking fault in (a).

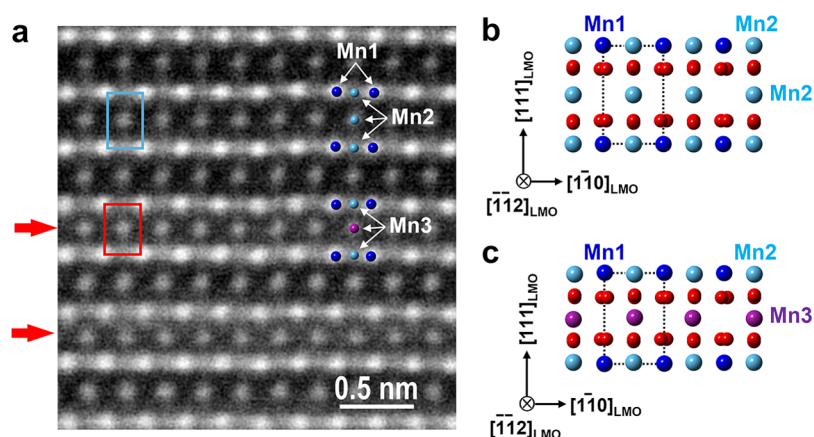


Figure 9. (a) High-resolution HAADF STEM image of (111) stacking faults (indicated by red arrows) in $\text{Li}_x\text{Mn}_2\text{O}_4$ ($\alpha \approx 0$) after five charge cycles, observed down $[\bar{1}\bar{1}2]_{\text{LMO}}$; the light-blue and red rectangles indicate the repeat units of a spinel layer and stacking fault layer, respectively, together with the corresponding atom models. (b) Columns of Mn and O atoms in spinel-structured $\text{Li}_x\text{Mn}_2\text{O}_4$ ($\alpha \approx 0$) observed down $[\bar{1}\bar{1}2]_{\text{LMO}}$. (c) Columns of Mn and O atoms observed along $[\bar{1}\bar{1}2]_{\text{LMO}}$ in a stacking fault layer formed by Mn2 atoms in the spinel structure occupying rock-salt type positions as in Figure 7c. The structures in (b) and (c) appear identical apart from the contraction of the stacking fault layer in the $[111]_{\text{LMO}}$ direction. Mn1 atoms are dark blue, Mn2 atoms are light blue, Mn3 atoms are purple, and O atoms are red.

is about $0.865 \times d(111)_{\text{LMO}}$, which corresponds to a volume contraction of 13.5%. Oblique stacking faults originating from steps on the Au surface with (111) orientation were confirmed to have identical structures (Figure S1 of Supporting Information). The marked increase in the number of stacking faults between the first and fifth charges indicates that point defects in the crystal lattice accumulate as Li is removed and re-enters the structure, even though the stacking faults were all removed after the first cycle. At some point between the first and fifth charges, this accumulation results in the creation and annihilation of stacking faults no longer being reversible (Figure 5). Repeated anisotropic expansion and contraction of the structure at these high levels ($\Delta\text{vol} > 10\%$), particularly as the stacking faults increase in number, can be expected to induce cracks that lead to exfoliation of surface layers and, ultimately, the mechanical failure of the LMO thin film. In particles of LiMn_2O_4 this typically occurs after some tens of cycles,¹⁰ but may take longer in the case of these thin films owing to the constraining effect of the Au/ Al_2O_3 substrate.

Figure 9a shows a HAADF image of stacking faults viewed down the $[\bar{1}\bar{1}2]_{\text{LMO}}$ zone axis, with structure models of the spinel matrix and the stacking fault structure viewed down the same direction in Figure 9b and Figure 9c, respectively. Down this direction, the spinel layers and stacking faults appear the same, apart from the compression of the latter in the $[111]_{\text{LMO}}$ direction and slightly higher background contrast, which are indicative of greater lattice strain. We note that the stacking fault structure is reminiscent of, but not identical to, that of rutile $\beta\text{-MnO}_2$; a comparison of these structures is given in Figure 10.^{54,55}

Density functional theory calculations of rutile-structured $\beta\text{-MnO}_2$ ⁵⁶ showed that Li-ion migration in such a structure occurs primarily parallel to $[001]$ (i.e., one-dimensionally), with an energy barrier of only 0.17 eV compared to 7.33 eV parallel to $[100]$. In spinel LMO, Li ions migrate in $\langle 111 \rangle$ directions; in the case of our thin films, the $(11\bar{1})_{\text{LMO}}$ plane is inclined at 70° to the Au(111) substrate surface and the $(111)_{\text{LMO}}$ planes parallel to it. In the case of the latter, the $[001]_{\text{R}}$ direction of the rutile-like structure is parallel to $[\bar{1}\bar{1}0]_{\text{LMO}}$, i.e., it lies parallel to the stacking fault layer (Figure 9), and $[100]_{\text{R}}$ is perpendicular to it. Assuming that Li-ion

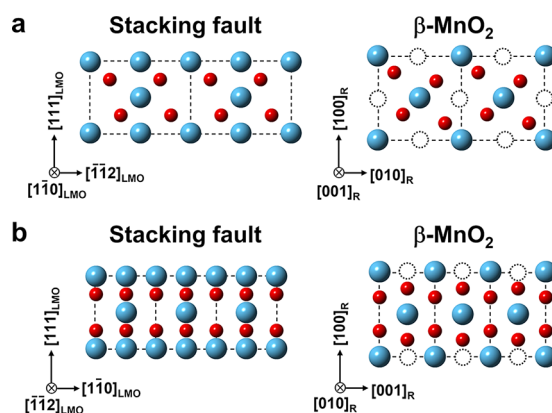


Figure 10. Comparison of $\{111\}$ stacking fault and rutile $\beta\text{-MnO}_2$ structures viewed down $[110]_{\text{LMO}}$ and $[001]_{\text{R}}$ directions (a) and viewed down $[\bar{1}\bar{1}2]_{\text{LMO}}$ and $[010]_{\text{R}}$ directions (b). Large blue balls are Mn, and small red balls are oxygen. Dashed circles indicate sites occupied by Mn in the stacking fault structure.

migration through the stacking fault layer is similar to that in the rutile structure, this suggests that stacking faults parallel to the film-substrate interface strongly block Li-ion migration from the interior to the surface and then to the electrolyte (however, oblique stacking faults may be less blocking). Furthermore, the smaller volume of the stacking layers compared to $\beta\text{-MnO}_2$ may result in an even larger activation energy for migration across them. As the number of stacking faults parallel to the substrate was observed to be much greater than the number oblique to it after only a few cycles, the overall effect is expected to be an increase in film resistance with increasing number of cycles, which is consistent with the increase in thin film resistance with cycle number in Table 1. The formation of stacking faults thus appears to be the major cause of the increased resistance of the film during cycling, which is another factor contributing to the capacity fade.

We also examined the intersections between pairs of stacking faults. Figure 11 shows a HAADF image of a region of the thin film where a lateral (111) stacking fault (parallel to the substrate) and an oblique $(11\bar{1})$ stacking fault (at $\sim 70^\circ$ to the substrate) intersect. It can be seen that the oblique stacking

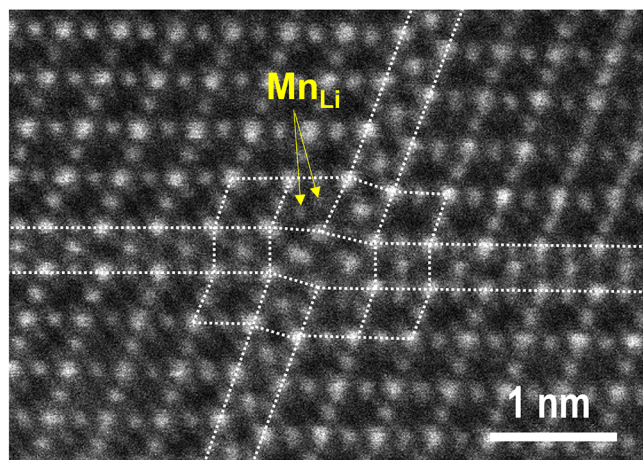


Figure 11. HAADF image taken down $[1\bar{1}0]_{\text{LMO}}$ of a LiMn_2O_4 epitaxial film after the fifth charge to 4.2 V (@1 mV/s) showing an intersection between stacking faults. Dotted lines demarcate the stacking fault layers and Mn diamonds adjacent to the intersection. Arrows point to contrast suggestive of Mn_{Li} antisite defects.

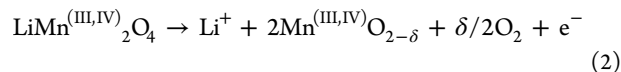
fault shifts by one repeat unit across the intersection, whereas the lateral stacking fault is only shifted by a fraction of this. The reason for this difference is not known, but it may be related to the presence of Mn_{Li} cation-site exchange defects next to the upper branch of the oblique stacking fault as indicated by arrows in the figure. The HAADF image reveals the high degree of coherency of the stacking fault layers even at their intersections, with the largest amount of structural distortion observed at the crossover point.

3.5. EELS Analysis of Stacking Faults. In addition to direct observation of the crystal structure by STEM, EELS analysis was performed using an aberration-corrected and monochromated probe to shed light on the local compositional changes during charge/discharge. Figure 12 shows the background-subtracted EELS spectra of the Li-K (together with Mn- $M_{2,3}$), O-K, and Mn- $L_{2,3}$ signals taken from the pristine film (black line; S0), the single-charged film (blue line; S1^c), and from a region of the film containing stacking faults after the fifth charge (red line; S1^{sf}). In the single-charged film, the Li-K signal becomes virtually undetectable in the bulk region (Figure 6b) compared to that in the pristine film (Figure 6a), which is consistent with its low Li content after their extraction into the electrolyte.

Quantitative EELS analysis using the white-line ratio method^{24,57} revealed that the average valence state of Mn

increased from about 3.48 in the pristine film to about 3.90 after a single charge, which is consistent with the increased pre-peak intensity of the corresponding O-K edge. This suggests that the average composition of the film interior after a single charge was close to that of MnO_2 (i.e., $\text{Li}_x\text{Mn}_2\text{O}_4$ where $x \approx 0$), which is consistent with near-complete delithiation. The EELS analysis of stacking fault layers, however, revealed a composition that is slightly lower in O content (decreased O-K pre-peak intensity) and a lower valence state of Mn compared to the spinel matrix, i.e., $\text{MnO}_{2-\delta}$. Quantitative analysis gave a δ value in this case of about 0.35,²⁴ although the actual δ value could be slightly larger if beam broadening effects are taken into account.

The EELS results show that the stacking faults contain a substantially higher concentration of oxygen vacancies than the spinel matrix, with many Mn atoms retaining a trivalent charge state. In other words, upon Li extraction, rather than the Mn^{3+} ions being oxidized to Mn^{4+} , removal of certain Li layers is compensated for by the formation of O^{2-} vacancies according to



MnO_6 octahedra with central Mn^{3+} atoms undergo strong Jahn–Teller distortion, and this strain likely drives the sliding of one part of the crystal to produce the -ABCBCABC-stacking sequence in the $[111]_{\text{LMO}}$ direction that is characteristic of the $\{111\}$ stacking faults. Although many of these stacking faults apparently disappear upon the reintercalation of Li (i.e., during discharge), with increasing numbers of cycles, some O and Mn vacancies most likely remain, their numbers increasing with the cycle number as damage to the crystal lattice accumulates. As mentioned in the previous section, this makes the formation of stacking faults easier as observed in our STEM images. A schematic summarizing the proposed formation mechanism of $\{111\}$ stacking faults based on the STEM and EELS results is provided in Figure S2 of the Supporting Information.

Observations of structural changes in LMO particles during electrochemical cycling reported in the literature suggest that similar degradation mechanisms are also active in other spinel-type cathode materials. For example, the formation of large numbers of stacking faults in LMO particles during cycling has been observed using conventional transmission electron microscopy and is associated with phase transformation to a double hexagonal type structure,¹¹ although the atomic structure could not be directly determined because of

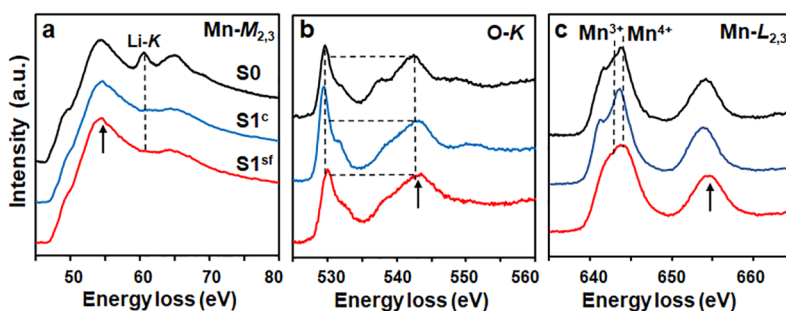


Figure 12. Background-subtracted EELS spectra of (a) Mn- $M_{2,3}$ (together with Li-K), (b) O-K, and (c) Mn- $L_{2,3}$ obtained from bulk regions of the pristine film (black lines; S0) and the single-charged film (blue lines; S1^c), and from stacking fault layers (red lines; S1^{sf}). Intensities of all profiles are normalized to those of the arrowed peaks.

technological limitations. The formation of cracks parallel to $\{111\}_{\text{LMO}}$ planes in electrochemically cycled LMO particles has also been studied recently,^{12,13} which is likely caused by the buildup of stress at the stacking faults after many cycles.

Reducing the number of stacking faults that form parallel to the substrate should thus be a priority for increasing the cyclability and reducing capacity fade in these materials in addition to taking measures to stabilize the surface structure.

4. CONCLUSIONS

Using advanced STEM methods, we observed the effects of Li deintercalation and intercalation at the atomic level in LiMn_2O_4 (LMO) epitaxial cathode thin films during charging and discharging of LMO/electrolyte/Li cells. Columns of Li atoms within Mn diamond units in pristine LiMn_2O_4 thin films viewed down $[1\bar{1}0]_{\text{LMO}}$ were visualized directly by ABF imaging. After charging the battery at 0.1 C to 4.2 V for the first time, Li atoms were confirmed to be removed from the structure to form $\lambda\text{-MnO}_2$ in the bulk of the film, but an Mn_3O_4 -like layer formed at the surface; Mn_3O_4 is known to be a poor Li conductor and thus contributes to increased cathode/electrolyte interface resistance. After discharge, columns of Li atoms again became visible with a return to the spinel LMO structure.

Fitting of impedance plots to equivalent circuit models indicated that in the charged state, the resistivity of the LMO/electrolyte interface increased, and this was correlated with the formation of Mn_{Li} defects at the surface of the LMO film. Further electrochemical cycling induced a number of $\{111\}$ stacking faults to propagate through the structure. These stacking faults were observed to be more compact than the spinel matrix and thus likely impede the intercalation of Li ions back into the cathodic thin film. Repeated volume expansion and contraction caused during cycling produced higher concentrations of stacking faults with a concomitant increase in film resistance. Further cycling is expected to lead to a further decrease in conductivity and capacity, not least because increasing lattice strain is expected to lead to crack formation and the eventual mechanical failure of the LMO thin film.

■ ASSOCIATED CONTENT

SI Supporting Information

The Supporting Information is available free of charge at <https://pubs.acs.org/doi/10.1021/acsami.1c18630>.

STEM micrographs and schematic of stacking fault formation mechanism (PDF)

■ AUTHOR INFORMATION

Corresponding Author

Yumi H. Ikuhara – Nanostructures Research Laboratory, Japan Fine Ceramics Center, Nagoya 456-8587, Japan; orcid.org/0000-0001-6634-0516; Email: yumi@jfcc.or.jp

Authors

Xiang Gao – Nanostructures Research Laboratory, Japan Fine Ceramics Center, Nagoya 456-8587, Japan; Present Address: Center for High Pressure Science and Technology Advanced Research, Beijing 100094, China
Kazuaki Kawahara – Institute of Engineering Innovation, The University of Tokyo, Tokyo 113-8656, Japan; orcid.org/0000-0002-8501-182X

Craig A. J. Fisher – Nanostructures Research Laboratory, Japan Fine Ceramics Center, Nagoya 456-8587, Japan; orcid.org/0000-0002-0999-5791

Akihide Kuwabara – Nanostructures Research Laboratory, Japan Fine Ceramics Center, Nagoya 456-8587, Japan; orcid.org/0000-0002-2810-3437

Ryo Ishikawa – Institute of Engineering Innovation, The University of Tokyo, Tokyo 113-8656, Japan; orcid.org/0000-0001-5801-0971

Hiroki Moriwake – Nanostructures Research Laboratory, Japan Fine Ceramics Center, Nagoya 456-8587, Japan

Yuichi Ikuhara – Nanostructures Research Laboratory, Japan Fine Ceramics Center, Nagoya 456-8587, Japan; Institute of Engineering Innovation, The University of Tokyo, Tokyo 113-8656, Japan; orcid.org/0000-0003-3886-005X

Complete contact information is available at:

<https://pubs.acs.org/10.1021/acsami.1c18630>

Author Contributions

Y.H.I. designed the experiments, and Y.H.I., X.G., K.K., and C.A.J.F. performed the experimental work and analyzed and interpreted the results. Y.H.I., X.G., and C.A.J.F. wrote the manuscript and prepared the figures. All authors discussed the results and commented on the manuscript.

Notes

The authors declare no competing financial interest.

■ ACKNOWLEDGMENTS

Part of this research was supported by JSPS KAKENHI grant no. JP21K04635 and Grants-in-Aid for Specially Promoted Research (grant no. JP17H06094) from JSPS. The authors thank Dr. Shunsuke Kobayashi and Mr. Yoshihiro Sugawara of Japan Fine Ceramics Center and Dr. Keiichi Kohama and Dr. Hideki Iba of Toyota Motor Corporation for valuable discussions.

■ REFERENCES

- (1) Goodenough, J. B.; Park, K. S. The Li-Ion Rechargeable Battery: A Perspective. *J. Am. Chem. Soc.* **2013**, *135*, 1167–1176.
- (2) Wu, F.; Maier, J.; Yu, Y. Guidelines and trends for next-generation rechargeable lithium and lithium-ion batteries. *Chem. Soc. Rev.* **2020**, *49*, 1569–1614.
- (3) Khan, S. A.; Shahid, A.; Saeed, K.; Usman, M.; Khan, I. Advanced cathode materials and efficient electrolytes for rechargeable batteries: practical challenges and future perspectives. *J. Mater. Chem. A* **2019**, *7*, 10159–10173.
- (4) Manthiram, A. A reflection on lithium-ion battery cathode chemistry. *Nat. Commun.* **2020**, *11*, 1550.
- (5) Yuan, Y. F.; Amine, K.; Lu, J.; Shahbazian-Yassar, R. Understanding materials challenges for rechargeable ion batteries with in situ transmission electron microscopy. *Nat. Commun.* **2017**, *8*, 15806.
- (6) Harper, G.; Sommerville, R.; Kendrick, E.; Driscoll, L.; Slater, P.; Stolkin, R.; Walton, A.; Christensen, P.; Heidrich, O.; Lambert, S.; Abbott, A.; Ryder, K.; Gaines, L.; Anderson, P. Recycling lithium-ion batteries from electric vehicles. *Nature* **2019**, *575*, 75–86.
- (7) Palacin, M. R. Understanding ageing in Li-ion batteries: a chemical issue. *Chem. Soc. Rev.* **2018**, *47*, 4924–4933.
- (8) Pender, J. P.; Jha, G.; Youn, D. H.; Ziegler, J. M.; Andoni, I.; Choi, E. J.; Heller, A.; Dunn, B. S.; Weiss, P. S.; Penner, R. M.; Mullins, C. B. Electrode Degradation in Lithium-Ion Batteries. *ACS Nano* **2020**, *14*, 1243–1295.
- (9) Fell, C. R.; Qian, D.; Carroll, K. J.; Chi, M.; Jones, J. L.; Meng, Y. S. Correlation Between Oxygen Vacancy, Microstrain, and Cation

Distribution in Lithium-Excess Layered Oxides During the First Electrochemical Cycle. *Chem. Mater.* **2013**, *25*, 1621–1629.

(10) Liu, T.; Dai, A.; Lu, J.; Yuan, Y.; Xiao, Y.; Yu, L.; Li, M.; Gim, J.; Ma, L.; Liu, J.; Zhan, C.; Li, L.; Zheng, J.; Ren, Y.; Wu, T.; Shahbazian-Yassar, R.; Wen, J.; Pan, F.; Amine, K. Correlation between manganese dissolution and dynamic phase stability in spinel-based lithium-ion battery. *Nat. Commun.* **2019**, *10*, 4721.

(11) Dupont, L.; Hervieu, M.; Rousse, G.; Masquelier, C.; Palacin, M. R.; Chabre, Y.; Tarascon, J. M. TEM Studies: The Key for Understanding the Origin of the 3.3 V and 4.5 V Steps Observed in LiMn₂O₄-based Spinel. *J. Solid State Chem.* **2000**, *155*, 394–408.

(12) Hao, X.; Lin, X.; Lu, W.; Bartlett, B. M. Oxygen Vacancies Lead to Loss of Domain Order, Particle Fracture, and Rapid Capacity Fade in Lithium Manganospinel (LiMn₂O₄) Batteries. *ACS Appl. Mater. Interfaces* **2014**, *6*, 10849–10857.

(13) Warburton, R. E.; Castro, F. C.; Deshpande, S.; Madsen, K. E.; Bassett, K. L.; dos Reis, R.; Gewirth, A. G.; Dravid, V. P.; Greeley, J. Oriented LiMn₂O₄ Particle Fracture from Delithiation-Driven Surface Stress. *ACS Appl. Mater. Interfaces* **2020**, *12*, 49182–49191.

(14) Thackeray, M. M.; David, W. I. F.; Bruce, P. G.; Goodenough, J. B. Electrochemical Extraction of Lithium from LiMn₂O₄. *Mater. Res. Bull.* **1983**, *18*, 461–472.

(15) Ohzuku, T.; Kitagawa, M.; Taketsugu, H. Electrochemistry of Manganese Dioxide in Lithium Nonaqueous Cell: III. X-Ray Diffractional Study on the Reduction of Spinel-Related Manganese Dioxide. *J. Electrochem. Soc.* **1990**, *137*, 769–775.

(16) Tarascon, J. M.; McKinnon, W. R.; Coowar, F.; Bowmer, T. N.; Amatucci, G.; Guyomard, D. Synthesis Conditions and Oxygen Stoichiometry Effects on Li Insertion into the Spinel LiMn₂O₄. *J. Electrochem. Soc.* **1994**, *141*, 1421–1431.

(17) Ohzuku, T.; Takeda, S.; Iwanaga, M. J. Solid-state redox potentials for Li[Me_{1/2}Mn_{3/2}]O₄ (Me: 3d-transition metal) having spinel-framework structures: a series of 5 volt materials for advanced lithium-ion batteries. *J. Power Sources* **1999**, *81–82*, 90–94.

(18) Zhong, Q.; Bonakdarpour, A.; Zhang, M.; Gao, Y.; Dahn, J. R. Synthesis and Electrochemistry of LiNi_xMn_{2-x}O₄. *J. Electrochem. Soc.* **1997**, *144*, 205–213.

(19) Xia, Y.; Zhou, Y.; Yoshio, M. Capacity fading on cycling of 4 V Li/LiMn₂O₄ cells. *J. Electrochem. Soc.* **1997**, *144*, 2593–2600.

(20) Thackeray, M. M. Manganese oxides for lithium batteries. *Prog. Solid State Chem.* **1997**, *25*, 1–71.

(21) Zhan, C.; Wu, T.; Lu, J.; Amine, K. Dissolution, migration, and deposition of transition metal ions in Li-ion batteries exemplified by Mn-based cathodes. *Energy Environ. Sci.* **2018**, *11*, 243–257.

(22) Hirayama, M.; Ido, H.; Kim, K.-S.; Cho, W.; Tamura, K.; Mizuki, J.; Kanno, R. Dynamic Structural Changes at LiMn₂O₄/Electrolyte Interface during Lithium Battery Reaction. *J. Am. Chem. Soc.* **2010**, *132*, 15268–15276.

(23) Gao, X.; Ikuhara, Y. H.; Fisher, C. A. J.; Huang, R.; Kuwabara, A.; Moriwake, H.; Kohama, K.; Ikuhara, Y. Oxygen loss and surface degradation during electrochemical cycling of lithium-ion battery cathode material LiMn₂O₄. *J. Mater. Chem. A* **2019**, *7*, 8655–8854.

(24) Gao, X.; Ikuhara, Y. H.; Fisher, C. A. J.; Moriwake, H.; Kuwabara, A.; Oki, H.; Kohama, K.; Yoshida, R.; Huang, R.; Ikuhara, Y. Structural Distortion and Compositional Gradients Adjacent to Epitaxial LiMn₂O₄ Thin Film Interfaces. *Adv. Mater. Interfaces* **2014**, *1*, 1400143.

(25) Gummow, R.; De Kock, A.; Thackeray, M. Improved capacity retention in rechargeable 4 V lithium/lithium-manganese oxide (spinel) cells. *Solid State Ionics* **1994**, *69*, 59–67.

(26) Zhuo, Z.; Olalde-Velasco, P.; Chin, T.; Battaglia, V.; Harris, S. J.; Pan, F.; Yang, W. Effect of excess lithium in LiMn₂O₄ and Li_{1.15}Mn_{1.85}O₄ electrodes revealed by quantitative analysis of soft X-ray absorption spectroscopy. *Appl. Phys. Lett.* **2017**, *110*, No. 093902.

(27) Banerjee, A.; Shilina, Y.; Ziv, B.; Ziegelbauer, J. M.; Luski, S.; Aurbach, D.; Halalay, I. C. On the Oxidation State of Manganese Ions in Li-Ion Battery Electrolyte Solutions. *J. Am. Chem. Soc.* **2017**, *139*, 1738–1741.

(28) Amos, C. D.; Roldan, M. A.; Varela, M.; Goodenough, J. B.; Ferreira, P. J. Revealing the Reconstructed Surface of Li[Mn₂]O₄. *Nano Lett.* **2016**, *16*, 2899–2906.

(29) Bates, J. B.; Dudney, N. J.; Neudecker, B.; Ueda, A.; Evans, C. D. Thin-Film Lithium and Lithium-Ion Batteries. *Solid State Ionics* **2000**, *135*, 33–45.

(30) Dudney, N. J.; Bates, J. B.; Zuhr, R. A.; Young, S.; Robertson, J. D.; Jun, H. P.; Hackney, S. A. Nanocrystalline Li_xMn_{2-y}O₄ Cathodes for Solid-State Thin-Film Rechargeable Lithium Batteries. *J. Electrochem. Soc.* **1999**, *146*, 2455–2464.

(31) Xia, Q.; Zhang, Q.; Sun, S.; Hussain, F.; Zhang, C.; Zhu, X.; Meng, F.; Liu, K.; Geng, H.; Xu, J.; Zan, F.; Wang, P.; Gu, L.; Xia, H. Tunnel Intergrowth Li_xMnO₂ Nanosheet Arrays as 3D Cathode for High-Performance All-Solid-State Thin Film Lithium Microbatteries. *Adv. Mater.* **2021**, *33*, 2003524.

(32) Xia, Q.; Sun, S.; Xu, J.; Feng, Z.; Yue, J.; Zhang, Q.; Gu, L.; Xia, H. Self-Standing 3D Cathodes for All-Solid-State Thin Film Lithium Batteries with Improved Interface Kinetics. *Small* **2018**, *14*, 1804149.

(33) Iriyama, Y.; Nishimoto, K.; Yada, C.; Abe, T.; Ogumi, Z.; Kikuchi, K. J. *Electrochem. Soc.* **2006**, *153*, A821–A825.

(34) Kuwata, N.; Kumar, R.; Toribami, K.; Suzuki, T.; Hattori, T.; Kawamura, J. Thin film lithium ion batteries prepared only by pulsed laser deposition. *Solid State Ionics* **2006**, *177*, 2827–2832.

(35) Hirayama, M.; Sonoyama, N.; Ito, M.; Minoura, M.; Mori, D.; Yamada, A.; Tamura, K.; Mizuki, J.; Kanno, R. Characterization of Electrode/Electrolyte Interface with X-Ray Reflectometry and Epitaxial-Film LiMn₂O₄ Electrode. *J. Electrochem. Soc.* **2007**, *154*, A1065–A1072.

(36) Tang, S. B.; Xia, H.; Lai, M. O.; Lu, L. Characterization of LiMn₂O₄ thin films grown on Si substrates by pulsed laser deposition. *J. Alloys Compd.* **2008**, *449*, 322–325.

(37) Sonoyama, N.; Iwase, K.; Takatsuka, H.; Matsumura, T.; Imanishi, N.; Takeda, Y.; Kanno, R. Electrochemistry of LiMn₂O₄ epitaxial films deposited on various single crystal substrates. *J. Power Sources* **2009**, *189*, 561–565.

(38) Hendriks, R.; Cunha, D. M.; Singh, D. P.; Huijben, M. Enhanced Lithium Transport by Control of Crystal Orientation in Spinel LiMn₂O₄ Thin Film Cathodes. *ACS Appl. Energy Mater.* **2018**, *1*, 7046–7051.

(39) Shui, J. L.; Jiang, G. S.; Xie, S.; Chen, C. H. Thin films of lithium manganese oxide spinel as cathode materials for secondary lithium batteries. *Electrochim. Acta* **2004**, *49*, 2209–2213.

(40) Mohamedi, M.; Takahashi, D.; Itoh, T.; Umeda, M.; Uchida, I. ESD Fabricated Thin Films of Spinel LiMn₂O₄ for Lithium Microbatteries. I. Effects of Thickness. *J. Electrochem. Soc.* **2002**, *149*, A19–A25.

(41) Ikuhara, Y. H.; Gao, X.; Huang, R.; Fisher, C. A. J.; Kuwabara, A.; Moriwake, H.; Kohama, K.; Ikuhara, Y. Epitaxial Growth of LiMn₂O₄ Thin Films by Chemical Solution Deposition for Multilayer Lithium-Ion Batteries. *J. Phys. Chem. C* **2014**, *118*, 19540–19547.

(42) ten Elshof, J. E. Chemical solution deposition techniques for epitaxial growth of complex oxides, Chap. 4 (pp. 69–93) in “Epitaxial Growth of Complex Metal Oxides,” Edited by Koster, G.; Huijben, M.; Rijnders, G. 2015, Woodhead Publishing Cambridge: UK.

(43) Findlay, S. D.; Shibata, N.; Sawada, H.; Okunishi, E.; Kondo, Y.; Yamamoto, T.; Ikuhara, Y. Robust atomic resolution imaging of light elements using scanning transmission electron microscopy. *Appl. Phys. Lett.* **2009**, *95*, 191913.

(44) Findlay, S. D.; Shibata, N.; Sawada, H.; Okunishi, E.; Kondo, Y.; Yamamoto, T.; Ikuhara, Y. Dynamics of annular bright field imaging in scanning transmission electron microscopy. *Ultramicroscopy* **2010**, *110*, 903.

(45) Karim, A.; Fosse, S.; Persson, K. A. Surface structure and equilibrium particle shape of the LiMn₂O₄ spinel from first-principles calculations. *Phys. Rev. B* **2013**, *87*, No. 075322.

(46) Kawahara, K.; Ishikawa, R.; Higashi, T.; Kimura, T.; Ikuhara, Y. H.; Shibata, N.; Ikuhara, Y. Unique fitting of electrochemical impedance spectra by random walk Metropolis Hastings algorithm. *J. Power Sources* **2018**, *403*, 184–191.

(47) Kawahara, K.; Ishikawa, R.; Nakayama, K.; Higashi, T.; Kimura, T.; Ikuhara, Y. H.; Shibata, N.; Ikuhara, Y. Fast Li-ion conduction at grain boundaries in (La,Li)NbO₃ polycrystals. *J. Power Sources* **2019**, *441*, 227187.

(48) Huang, R.; Ikuhara, Y. H.; Mizoguchi, T.; Findlay, S. D.; Kuwabara, A.; Fisher, C. A. J.; Moriwake, H.; Oki, H.; Hirayama, T.; Ikuhara, Y. Direct Observation of Light Elements in Li_{1-x}Mn₂O_{4-δ} Lithium Battery Cathode Material. *Angew. Chem., Int. Ed.* **2011**, *50*, 3053–3057.

(49) Aurbach, D.; Levi, M.; Gamulski, K.; Markovsky, B.; Salitra, G.; Levi, E.; Heider, U.; Heider, L.; Oesten, R. Capacity fading of Li_xMn₂O₄ spinel electrodes studied by XRD and electroanalytical techniques. *J. Power Sources* **1999**, *81*, 472–479.

(50) Tang, D.; Sun, Y.; Yang, Z.; Ben, L.; Gu, L.; Huang, X. Surface Structure Evolution of LiMn₂O₄ Cathode Material upon Charge/Discharge. *Chem. Mater.* **2014**, *26*, 3535–3543.

(51) Li, W.; Dolocan, A.; Oh, P.; Celio, H.; Park, S.; Cho, J.; Manthiram, A. Dynamic behaviour of interphases and its implication on high-energy-density cathode materials in lithium-ion batteries. *Nat. Commun.* **2017**, *8*, 14589.

(52) Ma, J.; Hu, P.; Cui, G.; Chen, L. Surface and Interface Issues in Spinel LiNi_{0.5}Mn_{1.5}O₄: Insights into a Potential Cathode Material for High Energy Density Lithium Ion Batteries. *Chem. Mater.* **2016**, *28*, 3578–3606.

(53) Takahashi, I.; Kiuchi, H.; Ohma, A.; Fukunaga, T.; Matsubara, E. Cathode Electrolyte Interphase Formation and Electrolyte Oxidation Mechanism for Ni-Rich Cathode Materials. *J. Phys. Chem. C* **2020**, *124*, 9243–9248.

(54) Bolzan, A. A.; Fong, C.; Kennedy, B. J.; Howard, C. J. Powder Neutron Diffraction Study of Pyrolusite, β-MnO₂. *Aust. J. Chem.* **1993**, *46*, 939–944.

(55) Schilling, O.; Dahn, J. R. J. Thermodynamic Stability of Chemically Delithiated Li(Li_xMn_{2-x})O₄. *J. Electrochem. Soc.* **1998**, *145*, 569–575.

(56) Tompsett, D. A.; Parker, S. C.; Bruce, P. G.; Islam, M. S. Nanostructuring of β-MnO₂: The Important Role of Surface to Bulk Ion Migration. *Chem. Mater.* **2013**, *25*, 536–541.

(57) Varela, M.; Oxley, M.; Luo, W.; Tao, J.; Watanabe, M.; Lupini, A. R.; Pantelides, S.; Pennycook, S. Atomic-resolution imaging of oxidation states in manganites. *Phys. Rev. B* **2009**, *79*, No. 085117.

Recommended by ACS

Nanoscaled LiMn₂O₄ for Extended Cycling Stability in the 3 V Plateau

Valerie Siller, Albert Tarancón, *et al.*

JULY 13, 2022
ACS APPLIED MATERIALS & INTERFACES

READ 

Layered O6/O3 Multi-Phase Composite Derived from the P2/O3 Nanocrystalline Composite for High-Performance Li-Rich Manganese-Based Cathode Material

Wenyan Yang, Shengzhou Chen, *et al.*

AUGUST 23, 2022
ACS APPLIED ENERGY MATERIALS

READ 

Enhancing Structural Stability and Electrochemical Properties of Co-Less Ni-Rich Layer Cathode Materials by Fluorine and Niobium Co Doping

Zhongyuan Luo, Ke Du, *et al.*

SEPTEMBER 05, 2022
ACS APPLIED ENERGY MATERIALS

READ 

Bimodal AFM-Based Nanocharacterization of Cycling-Induced Topographic and Mechanical Evolutions of LiMn₂O₄ Cathode Films

Peifa Yang, Guangyi Shang, *et al.*

MAY 17, 2021
LANGMUIR

READ 

Get More Suggestions >